Conformation and translational diffusion of a xanthan polyelectrolyte chain: Brownian dynamics simulation and single molecule tracking

Myung-Suk Chun,[1,*] Chongyoup Kim,[2] and Duck E. Lee[1]
[1]*Complex Fluids Research Laboratory, Korea Institute of Science and Technology (KIST), Seongbuk-gu, Seoul 136-791, Republic of Korea*
[2]*Department of Chemical and Biological Engineering, Korea University, Seongbuk-gu, Seoul 136-713, Republic of Korea*
(Received 9 September 2008; revised manuscript received 19 February 2009; published 27 May 2009)

In our recent Brownian dynamics (BD) simulation study, the structure and dynamics of anionic polyelectrolyte xanthan in bulk solution as well as confined spaces of slitlike channel were examined by applying a coarse-grained model with nonlinear bead-spring discretization of a whole chain [J. Jeon and M.-S. Chun, J. Chem. Phys. **126**, 154904 (2007)]. This model goes beyond other simulations as they did not consider both long-range electrostatic and hydrodynamic interactions between pairs of beads. Simulation parameters are obtained from the viscometric method of rheology data on the native and sonicated xanthan polysaccharides, which have a contour length less than 1 μm. The size of the semiflexible polyelectrolyte can be well described by the wormlike chain model once the electrostatic effects are taken into account by the persistence length measured at a long length scale. For experimental verifications, single molecule visualization was performed on fluorescein-labeled xanthan using an inverted fluorescence microscope, and the motion of an individual molecule was quantified. Experimental results on the conformational changes in xanthan chain in the electrolyte solution have a reasonable trend to agree with the prediction by BD simulations. In the translational diffusion induced by the Debye screening effect, the simulation prediction reveals slightly higher values compared to those of our measurements, although it agrees with the literature data. Considering the experimental restrictions, our BD simulations are verified to model the single polyelectrolyte well.

DOI: 10.1103/PhysRevE.79.051919 PACS number(s): 87.15.Vv, 83.10.Mj, 82.35.Rs, 87.80.Nj

I. INTRODUCTION

Polyelectrolytes are distinguished from neutral polymers and have the ability to dissociate charges in poor solvents which results in charged polymer chains (macroion) and mobile counterions. They represent an interesting and broad class of soft matter that should be considered as an additional complication arising from the Debye screening of long-range electrostatic interaction by ions [1–3]. These characteristics prevent a direct application of many reliable theories developed for neutral polymers [4–7], and it is usually necessary to consider more system-specific aspects such as the linear charge density of chain, the ionic strength of the solution, and the condensation of counterions and salt ions. A thorough understanding of charged soft matter has become of great attention in life science and molecular biology because virtually all proteins, and other biopolymers such as DNA, polysaccharide, or microtubules, are polyelectrolytes.

Modeling studies using the Brownian dynamics (BD) method with hydrodynamic interaction (HI) have improved the understanding of how a single polyelectrolyte chain behaves when either exists in unbounded spaces or confined to channels. In modeling the properties of the polyelectrolyte solution, the solvent is typically treated as a continuum, while the molecule is usually represented by a coarse-grained model such as a bead-spring chain [8–10]. For the model polyelectrolyte, the use of biological macromolecules makes the study of monodisperse samples possible. Previous studies were almost confined to an analysis of the equilibrium conformation and the diffusion of a single DNA molecule, where its contour length is above 4 μm. This is based on the advancement of microfluidic or nanofluidic devices for DNA separation and gene mapping. For the study of confined DNA molecules, Jenderajack *et al.* [11,12] used a BD simulation coupled with a numerical solver for the solvent motion. They found the effect of a length scale associated with polymer-wall interactions because the scalings obtained did not match the theoretical predictions in square channels. Chen *et al.* [13] examined the diffusion of double stranded (ds)-DNA molecules in slitlike channels with variations in channel height and molecular weight.

On the experimental side, the shape and dynamics of fluorescein-labeled DNA molecules were investigated at the single molecule level in bulk solutions [14,15] as well as adsorbed to fluid cationic supported membranes with two dimensions [16–18]. The direct observation of molecular motion by epi-fluorescence microscopy takes some essential advantages of the relatively simple experimental setup and access to single molecule trajectories. Using the fluorescence microscopy, the trajectories of small fluorescein-labeled molecules can be followed. Recently, the diffusivity of ds-DNA in structures ranging from three dimensions to quasi-two-dimensions was measured [19], and the systematic investigation of its conformation and chain relaxation was performed in quasi-two-dimensional (2D) confinement of the Kuhn length (110 nm) [20].

Very recently, Jeon and Chun [21] developed coarse-grained models of polysaccharide xanthan polyelectrolytes in bulk solution as well as under confinement, taking into account the HIs between pairs of beads. Xanthan is generally accepted as a semiflexible polyelectrolyte due to the double

*mschun@kist.re.kr

stranded structure with intrinsic persistence length of at least 100 nm [22–24]. It has up to two ionizable carboxyl groups per repeat unit, and the side chains give a semirigid character to the main chain. The authors have studied the structural transition of a polyelectrolyte chain from unbounded to confined states with emphasis on the influence of chain intrinsic rigidity and the ionic strength of the surrounding medium. It revealed that the reduction in chain size at an intermediate confinement is accompanied by a severe loss of the long-range bond vector correlation measured by the persistence length at a long length scale.

Studies on the comparison between simulation and experimental data for single xanthan molecule have not been performed even in the case of bulk solution. Since the epifluorescence microscopy allows one to observe dynamic changes in xanthan molecules, single molecule tracking can promisingly provide insight into local fluctuations. It is the aim of this paper to verify our BD simulations by conducting accurate measurements and comparing with the experimental results on the conformation and diffusion of single xanthan molecules. As the model sample, both the native and sonicated xanthan are adopted in bulk solution, and the influence of the medium ionic strength is highlighted. Our results serve as a basis for further understanding the transport and manipulation of polyelectrolyte complex fluids in confined spaces, which has practical relevance in such research fields as microfluidics or nanofluidics, lab-on-chips, and single molecule or cell detection. Although the general trend of the data is in qualitative agreement, the experimental results do not show the full agreement with the simulation results of the translational diffusion. To bridge the gap between theory and experiment, we discuss the factors of the discrepancy.

II. BROWNIAN DYNAMICS SIMULATION OF XANTHAN POLYELECTROLYTE

A. Coarse-grained modeling

Here, a brief review is provided regarding the coarse-grained mesoscopic model of polyelectrolytes with polysaccharide xanthan and the BD simulation method employed in the prior work [21], in which the xanthan was modeled as a bead-spring chain composed of uniformly charged monomers. The generalized Langevin equation provides the reference for the generation of molecular trajectories in a dielectric continuum of the solvent medium.

The dynamics of xanthan chain is described by the following BD equation of motion that accounts for the bead-bead fluctuating HI through the first-order Ermak and McCammon algorithm [25],

$$\mathbf{r}_i^{n+1} = \mathbf{r}_i^n + \Delta t \sum_j \frac{\mathbf{D}_{ij}^n \cdot \mathbf{F}_j^n}{k_B T} + \Delta t \sum_j \nabla_j \cdot \mathbf{D}_{ij}^n + \mathbf{R}_i^n, \tag{1}$$

where subscripts i and j represent each bead. $\mathbf{F}_j^n = -\nabla E^{\text{Total}}(t_n)$ is the total force on bead at time step n, $\mathbf{R}_i^n$ is the random displacement due to the solvent, Δt is the time step size, and $k_B T$ is the Boltzmann thermal energy. The velocity field created from the motion of a segment of the xanthan molecule is taken to be due to a chain of point forces acting on the fluid. The bead-bead HI is adequately represented by a chain of point forces (Stokeslets). Here, the Rotne-Prager diffusion tensor $\mathbf{D}_{ij}^n$ is employed to describe the HI between beads [26], which is positive definite for all chain configurations. It can be expressed as

$$\mathbf{D}_{ij} = k_B T \left(\frac{1}{6\pi\eta a} \mathbf{I} \delta_{ij} + \mathbf{\Omega}_{ij} \right), \tag{2}$$

where η is the solvent viscosity, $\mathbf{I}$ is the 3×3 unit tensor, and $\mathbf{\Omega}_{ij}$ is the HI tensor which relates the velocity perturbation at point $\mathbf{r}_i$ to a point force at $\mathbf{r}_j$,

$$\mathbf{\Omega}_{ij} = \frac{1}{8\pi\eta r_{ij}} \left[\left(1 + \frac{2a^2}{3r_{ij}^2} \right) \mathbf{I} + \left(1 - \frac{2a^2}{r_{ij}^2} \right) \frac{\mathbf{r}_{ij}\mathbf{r}_{ij}}{r_{ij}^2} \right] \quad (i \neq j, r_{ij} > 2a), \tag{3a}$$

$$\mathbf{\Omega}_{ij} = \frac{1}{8\pi\eta r_{ij}} \left[\frac{r_{ij}}{2a} \left(\frac{8}{3} - \frac{3r_{ij}}{4a} \right) \mathbf{I} + \frac{r_{ij}^2}{8a^2} \frac{\mathbf{r}_{ij}\mathbf{r}_{ij}}{r_{ij}^2} \right] \quad (i \neq j, r_{ij} \leq 2a). \tag{3b}$$

Brownian forces are coupled to these velocity perturbations through the fluctuation-dissipation theorem, and the distribution of $\mathbf{R}_i^n$ is Gaussian with zero mean and covariance, expressed as $\langle \mathbf{R}_i^n \mathbf{R}_j^n \rangle = 2\mathbf{D}_{ij}^n \Delta t$. Here, the integration time step Δt is chosen to satisfy the criterion $m_0/(6\pi\eta a) \ll \Delta t \ll 6\pi\eta a^3/k_B T$ for the bead mass m_0.

Springs with distance $r_{i,i+1}$ between neighboring beads i and $i+1$ are assured by the finitely extendable nonlinear elastic (FENE) potential of Warner [27],

$$E_{i,i+1}^{\text{FENE}} = -(k_S l_{\max}^2/2) \ln[1 - (r_{i,i+1} - l_0)^2/l_{\max}^2], \tag{4}$$

where l_0 is the equilibrium bond length and $l_{\max}$ is the maximum bond length allowed. E^{FENE} is reduced to a harmonic potential with force constant k_S, in the limit of large $l_{\max}$. The Lennard-Jones (LJ) potential describing the dispersion-repulsion interaction between pairs of beads is taken by considering the energy parameter ε_{LJ} and the length scale σ_{LJ} set equal to $1.0 k_B T$ and $1.0 l_0$, respectively. The electrostatic interaction between beads is described via the screening Coulombic interaction, usually known as the Debye-Hückel (DH, or Yukawa) potential,

$$E_{ij}^{\text{ES}} = \frac{q_b^2}{4\pi\varepsilon} \frac{e^{-\kappa r_{ij}}}{r_{ij}} = k_B T z_b^2 \frac{l_B}{r_{ij}} e^{-\kappa r_{ij}}. \tag{5}$$

Here, q_b means the bead charge, the medium dielectric constant $\varepsilon(=\varepsilon_r \varepsilon_0)$ is defined in terms of the relative permittivity $\varepsilon_r(=78.5)$ and vacuum permittivity $\varepsilon_0(=8.854 \times 10^{-12}\ \text{C}^2/\text{J m})$, $\kappa = (8\pi l_B N_A I)^{1/2}$ is the inverse Debye screening thickness determined by Avogadro's number N_A, medium ionic strength I, and the Bjerrum length $l_B = e^2/4\pi\varepsilon k_B T$ (cf., $l_B = 0.71$ nm in water at room temperature), and $z_b = q_b/e$ is the bead charge in units of elementary charge $e(=1.6 \times 10^{-19}\ \text{C})$. The finite rigidity of the chain is modeled by the following harmonic bending potential:

$$E_{i,i+1}^{\mathrm{Bend}} = (k_A \theta_{i,i+1}^2)/2, \tag{6}$$

where k_A is the bending force constant and $\theta_{i,i+1} = \cos^{-1}(\hat{b}_i \cdot \hat{b}_{i+1})$ with the ith bond vector of unit size $\hat{b}_i = (\mathbf{r}_{i+1} - \mathbf{r}_i)/|\mathbf{r}_{i+1} - \mathbf{r}_i|$. This study addresses both models with and without the bending potential between neighboring bonds, representing the semiflexible and flexible chains, respectively.

The approach of Chun and Park [24] supports the information for the dimension of native xanthan chain as the average molecular weight $\bar{M}_W$ of 1.13×10^6 g/mol (approximately 1220 monomers) with the persistence length $l_P \cong 120$ nm and the contour length $R_C \cong 580$ nm at ionic strength $I = 100$ mM. This chain is modeled as a mesoscopic discrete wormlike chain with 25 beads ($N_b = 25$), where about 10 beads represent a Kuhn segment of length $2l_P$ ensuring a smooth persistence length variation according to environmental conditions. The bead hydrodynamic radius a chosen as 5 nm is close to the value determined by taking the experimentally evaluated chain diameter d [23,28] and then equating the volume of a circular cylinder of such diameter and 580 nm length to the volume $[=(4\pi/3)(a^3 N_b)]$ of 25 beads.

Conducting the previously described scheme [21], spring parameters (k_S, l_0, $l_{\max}$, k_A) and z_b are optimized with preliminary BD simulations such that the chain reproduces experimental values of R_C and l_P at different solution ionic concentrations. We take the optimum stretching constant $k_S = 2.5 k_B T / l_0^2$, $l_0 = 10$ nm, and $l_{\max} = 150$ nm for semiflexible chain, and $k_S = 3 k_B T / l_0^2$, $l_0 = 18$ nm, and $l_{\max} = 40$ nm for flexible chain. Note that the weak spring constant employed here is not so much a signature of entropic spring as a convenient way to take into account the large ionic strength dependence of xanthan contour length. The optimal bead charges q_b of $-35e$ for semiflexible chain ($-30e$ for flexible chain) corresponds to $\sim 35\%$ of the maximum value of $-98e$ for the bead composed of 49 (=1220/25) monomers, which leads to the contour distance per elementary charge l_q ($=R_C/(N_b z_b)$) of 0.66 nm. According to the Manning condensation [6,29], the minimum possible value of l_q in the presence of monovalent counterions is the Bjerrum length l_B (0.71 nm), in agreement within 10%. Therefore, it does not need to consider counterions since the parametrized bead charges include the possibility of counterion condensation. The optimized angle bending force constant determined as $k_A = 4 k_B T$ yields $l_P = 4b$, where the average bond length b has the relation $l_P = b k_A/(k_B T)$ for a wormlike chain [9,30]. This is close to the simulation result, $l_P = 4.3b$ at $I = 100$ mM if $b = 2.4 l_0$ is taken.

B. Global properties

Structural properties of the xanthan chain can be the root-mean-square end-to-end distance R_E and radius of gyration R_G [31], given by

$$R_E = \langle (\mathbf{r}_{N_b} - \mathbf{r}_1)^2 \rangle^{1/2} = \left\langle \left(\sum_{n=1}^{N_b} \mathbf{r}_n \right)^2 \right\rangle^{1/2}, \tag{7}$$

$$R_G^2 = \frac{1}{N_b} \sum_{n=1}^{N_b} \langle |\mathbf{r}_n - \mathbf{R}_{CM}|^2 \rangle, \tag{8}$$

with the position of the center of mass

$$\mathbf{R}_{CM} = \left(\sum_{n=1}^{N_b} \mathbf{r}_n \right) / N_b. \tag{9}$$

The theoretical scaling for these properties is $\langle R_E^2 \rangle \propto \langle R_G^2 \rangle \propto (N_b - 1)^{2\nu}$, where the value of ν has 0.588 for a self-avoiding walk in good solvent from renormalization-group theory methods [32]. Further, the contour length R_C is given by

$$R_C = (N_b - 1) b = \sum_{n=1}^{N_b - 1} b_n = \sum_{n=1}^{N_b - 1} |\mathbf{r}_{n+1} - \mathbf{r}_n|, \tag{10}$$

where b_n is the nth bond length. Note that the contour length R_C can vary with medium ionic strength due to the variable screening of bead-bead electrostatic interactions. As described in detail in a previous study [21], the persistence length l_P can be determined from the average contour distance between beads separated by n bonds. The correlation length of bond vectors separated by n bonds, which provides a useful measure of the relative strength of short- and long-range bond vector correlations, becomes independent of n only when the bond vector correlation decays exponentially on the entire length scale. Under a given condition, 20 independent BD trajectories are analyzed for each of more than 10 ms in length.

A diffusive motion of the Brownian particle is parametrized by its translational self-diffusion coefficient through the Einstein-Smoluchowsky relation (within the framework of Kirkwood theory) [31,33],

$$D_{T,\beta} = \lim_{\delta t \to \infty} \frac{1}{2\delta t} \langle [R_{CM,\beta}(t) - R_{CM,\beta}(t - \delta t)]^2 \rangle \quad \text{for} \quad \beta = x, y, z. \tag{11}$$

Here, δt is the lag time and the average $\langle \cdots \rangle$ is the mean-square displacement (MSD) carried out over the entire trajectory. In order to better compare the experimental results with simulations, we consider the 2D diffusion coefficients $D_T^{2D} = (\Sigma_{\beta=x,y} D_{T,\beta})/2$ in bulk. In bulk solution, however, the full three-dimensional (3D) diffusion coefficient is found to be different from the 2D one with x and y components by less than 2%. In practice, the limit $\delta t \to \infty$ on the right-hand side of Eq. (11) is replaced by $\delta t = 0.2$ ms, from which the estimated error is less than 2% in the bulk solution and less than 5% under confinement.

III. EXPERIMENTAL DETAILS

A. Xanthan preparation: Native and sonicated samples

The powdered xanthan used in this study was purchased from Sigma Chemical Co. (St. Louis, MO). Care was taken during sample preparation to remove microgels, and the solutions containing nearly monodisperse samples were obtained by employing membrane filtrations. According to the

TABLE I. Determination of the persistence lengths and contour lengths of xanthan samples for different electrolyte concentrations.

		Persistence length, l_P (nm)		Contour length, R_C (nm)	
Ionic strength, I (mM)	$10^{-2}\kappa$ (nm^{-1})	Chun and Park [24] Yamakawa-Fujii [35]	OSF [36,37]	Native xanthan ($\bar{M}_W=1.13\times10^6$)	Sonicated xanthan[a] ($\bar{M}_W=6.9\times10^5$)
100	103.66	120 ± 10	105	580	360
4.0	20.73	150 ± 10	111	730	
1.0	10.37	160 ± 10	123	750	460
0.2	4.64	200 ± 10	167	880	
0.1	3.28	240 ± 10	240	960	590
0.01	1.04	460 ± 10	881		770

[a]Ultrasonication for 5 min.

degree of chain scission desired, xanthan fractions having different molecular weights or sizes can be prepared by ultrasonic degrading the native material without structural or chemical modification. In this study, sample solutions were exposed to 75 W of 23 kHz sound with a sonifier cell disruptor (Branson Model 450) for 5 min. From the peak analysis obtained by the capillary hydrodynamic fractionation, polydispersities for each sample prepared were found to be in the ranges between 1.1 and 1.4. The medium ionic strength was adjusted with KCl electrolyte using the deionized and distilled water with 18 MΩ cm resistance. The pH of the xanthan solution was maintained to about 6.2, where the change over an experimental time course was quite small (less than 6%) not to affect the medium ionic strength.

The average molecular weight $\bar{M}_W$ of 5 min sonicated xanthan is determined as 6.9×10^5 g/mol (approximately 745 monomers) by adopting the viscometric method incorporating the Mark-Houwink relation, likewise the case of the native xanthan. The contour length R_C has about 360 nm with $l_P\cong120$ nm at ionic strength of 100 mM, from the best fit of intrinsic viscosity $[\eta]$ data to the theoretical Yamakawa-Yoshizaki curves described in detail in the literature [24,34]. The contour lengths estimated for each sample and condition are summarized in Table I. It is remarkable that the obtained persistence lengths show a fair overall agreement with the predictions according to Odijk [35], Skolnick, and Fixman (OSF) [36]. The ionic concentration of the symmetric monovalent electrolyte equals the medium ionic strength, in which the Debye thickness κ^{-1}(nm) is given by (ionic strength I(M))$^{-1/2}$/3.278. In Fig. 1(a), the large increase in the experimentally observed R_C with decreasing κ [24] is well reproduced in native and sonicated xanthan. A similarly large change in R_C (i.e., 450 nm at I =0.5 M and 1651 nm in pure water) was reported from an atomic force microscope (AFM) study on dehydrated samples [37]. The extension of xanthan at low ionic strength and a corresponding increase in the solution viscosity are likely to involve a transition of the secondary structure (i.e., backbone conformation) from a double strand to a disordered form with lower strandedness [38]. This denatured xanthan can undergo a disorder→order (i.e., coil→helix) transition when sufficient salt is present. Figure 1(b) shows that the short degraded xanthan takes stiffer chains and the extended backbone of xanthan chains is accompanied by an increase in chain stiffness with decreasing I. As noted before, the xanthan with $R_C/l_P\geq3$ can be regarded as a continuous wormlike chain that is modeled as a discrete chain with 25 beads.

B. Fluorescein labeling and characterization

Following the procedure outlined by Holzwarth [39], both the native and sonicated xanthan were tagged by the attachment of a fluorescein derivative to a finite portion of the carboxyl groups found along the polymer backbone. The tag-

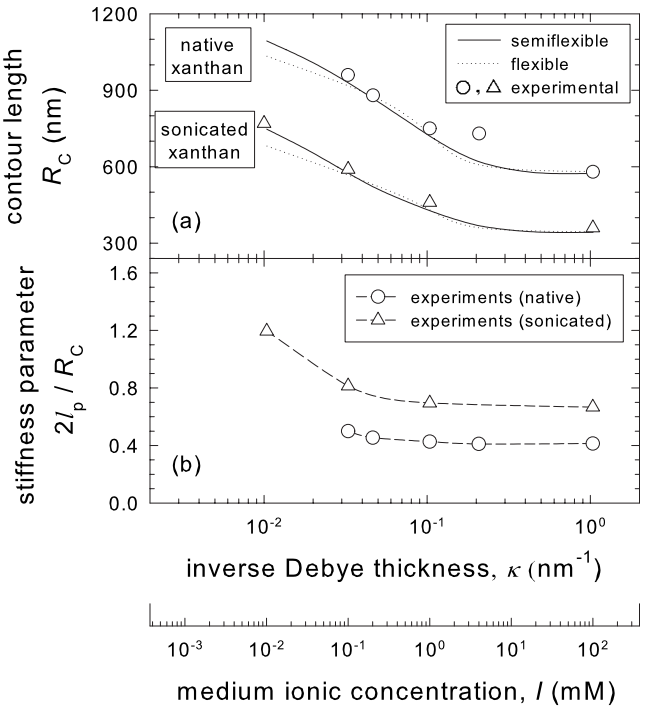

FIG. 1. The variations in (a) the contour length R_C and (b) the stiffness parameter of a single native and 5 min sonicated xanthan with Debye parameter κ in bulk solution. Experimental data are provided from this study as well as Ref. [24].

TABLE II. Zeta potential and electrophoretic mobility of xanthan samples for different amounts of fluorescein added to the 300 ml solution of 1000 ppm native xanthan.

5-amino fluorescein (mg)	None (unlabeled)	8	15	23	35
Zeta potential (mV)	−61.8	−53.6	−60.8	−62.4	−71.2
Mobility (10^{-4} cm^2/V·s)	−4.50	−3.94	−4.39	−4.55	−5.37

ging reaction is initiated by adding 15 mg 5-amino fluorescein and 60 μl cyclohexyl isocyanide to the 300 ml solution of 1000 ppm xanthan and a 50 ml dimethyl sulfoxide solution prepared with 60 μl acetaldehyde. The mixture is stirred at a low speed for 24 h at room temperature, and then the labeled xanthan is isolated by precipitation with 4 parts ethanol to 1 part reaction mixture, where 1 wt % NaCl is added. The purification process is repeated with a cycle of precipitation until all the residual-free dyes were washed off. Subsequently, the precipitated xanthan is redissolved in 2 g/L Triton X-100 and 2 mM sodium azide, and then dialyzed with ultrafiltration membrane (YM100, Millipore, MA) for 3 days against this solvent. Prepared samples of unlabeled and fluorescein-labeled xanthan were stored in a refrigerator until use with sufficiently dilute concentration ($\leq$100 ppm).

The degree of fluorescein labeling was found to be 0.5–1.0 wt %, determined by UV-Visible absorption spectrophotometry (S-3100, Scinco, Seoul). In order to identify the change in surface charge condition for different amounts of fluorescein dye, the zeta potential was estimated from the mobility values measured with an electrophoretic light-scattering spectrophotometer (ELS-8000, Otsuka Electronics, Osaka). In Table II, the magnitude of the negative zeta potential of the native xanthan is almost equivalent to that of the labeled one with 15 mg fluorescein, which was used in this study. Intrinsic viscosities were obtained by measuring shear viscosity carried out with a low-shear capillary viscometer of Ubbelohde type at room temperature. The electrostatic excluded-volume contribution in semiflexible polyelectrolyte solution accounts for the linear relationship between $[\eta]$ and κ^{-1} over a certain range, such as $[\eta] = [\eta]_{inf} + \alpha_e/\kappa$, where $[\eta]_{inf}$ is the intrinsic viscosity at sufficiently high ionic concentration ($I \geq 100$ mM) and the slope α_e is an extension coefficient [24]. Figure 2 shows that the intrinsic viscosity is reduced overall in the labeled xanthan, accompanying a decrease in the extension coefficients less than 20%.

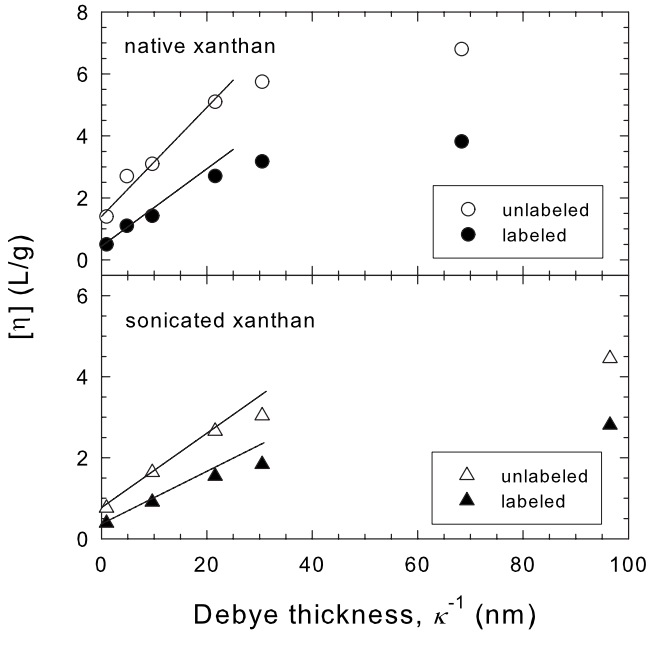

FIG. 2. Intrinsic viscosity vs κ^{-1} for native and 5 min sonicated xanthan. Solid lines provide a linear fit with the slope α_e holding over the suitable range.

C. Fluorescence microscopy

Fluorescein-labeled xanthan molecules were excited with an Hg laser at 450–500 nm and monitored with emission at 520 nm using an inverted epi-fluorescence microscope (Nikon, Eclipse Ti-E) with a 100× [numerical aperture (NA) of 1.3, resolution of 0.2 μm, focal depth of 0.41 μm] oil immersed objective, as depicted in Fig. 3. Images were taken by a digital 12 bit charge coupled device (CCD) camera (Nikon, Digital Sight DS-Qi1, monochrome cooled) with 30

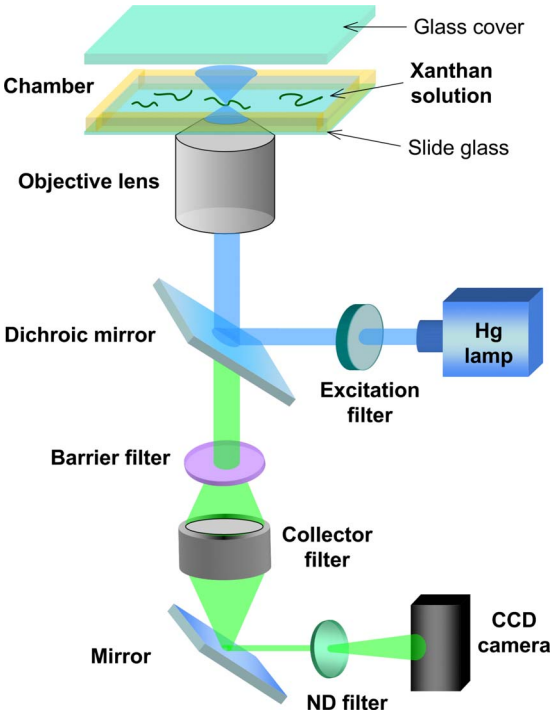

FIG. 3. (Color online) Schematic of inverted epi-fluorescence microscopy utilized in single molecule detection of xanthan.

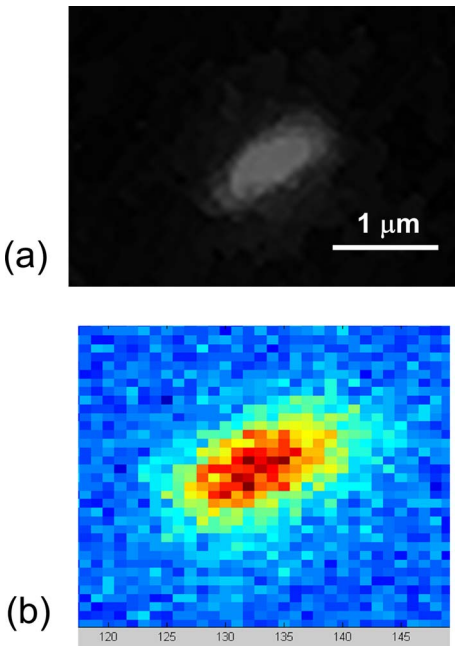

FIG. 4. (Color online) (a) A typical fluorescence image of native xanthan in KCl 0.1 mM solution, where the microscope was focused away at least 24 μm from the downside wall with the exposure time of 30 ms. (b) The pixel intensity of the fluorescence image.

ms exposure time recording 1280×1024 pixels. Under 100 $\times$ magnification, each image pixel corresponds to 65 nm. 160 frames over a period of 16 s were recorded for each xanthan molecule. The data acquisition was performed using the NIS-Elements software and image processing was accomplished by the MATLAB (Mathworks, MA).

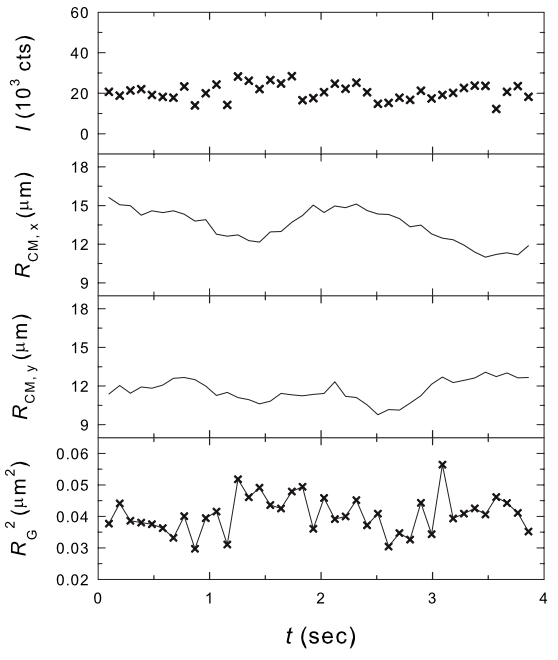

FIG. 5. Typical time evolution of the zeroth, first, and second moments of the intensity distribution of a single native xanthan molecule in KCl 1.0 mM solution. The time interval is 97 ms.

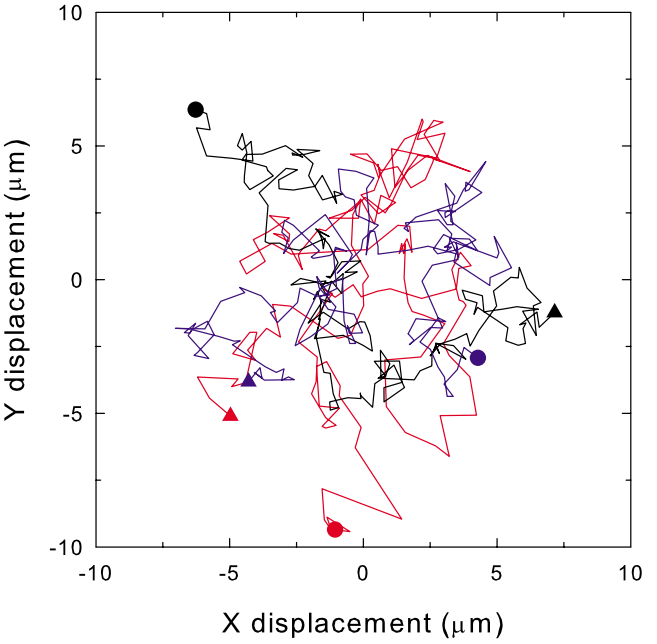

FIG. 6. (Color online) The center-of-mass trajectories of native xanthan molecules in KCl 1.0 mM solution during a sequence of images with 97 ms interval time. Filled circle and triangle symbols indicate the start and stop positions, respectively.

To provide the bulk space, a homemade chamber was prepared with slide glass and glass cover having 50 and 150 μm thicknesses, respectively. They were separated by 3 mm high polydimethylsiloxane (PDMS) frame, which was completely sealed. The chamber mounted on the microscope has dimensions of 60 mm by 24 mm in the x-y plane. The chamber volume of 4.3 ml is large enough not to be disturbed by temperature rise during the course of an experi-

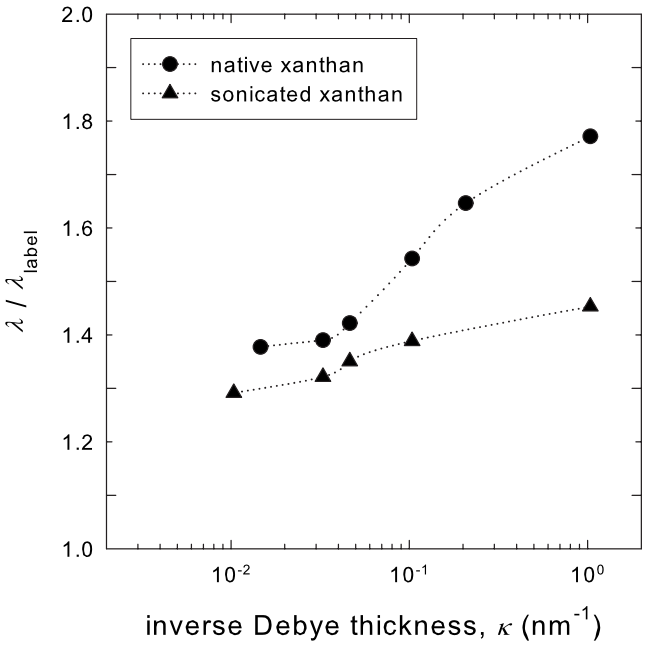

FIG. 7. The variations in $\lambda/\lambda_{\text{label}}$ of native and 5 min sonicated xanthan with Debye parameter κ in bulk solution.

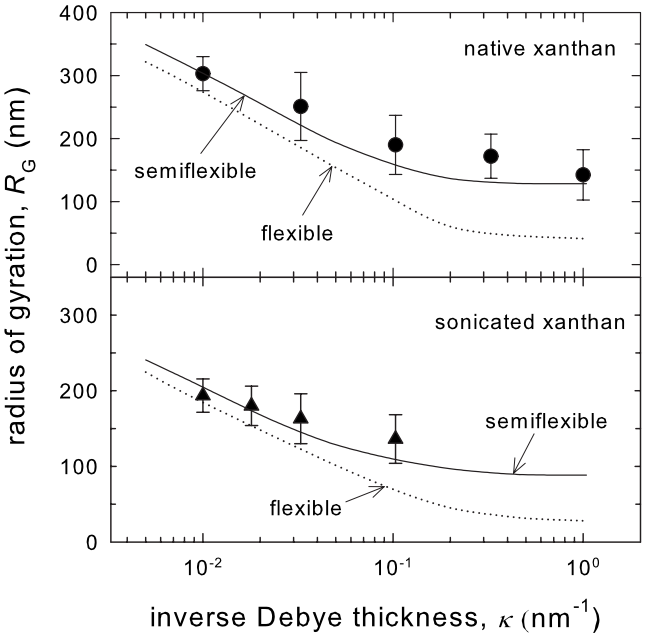

FIG. 8. The variations in the radius of gyration R_G of a single native and 5 min sonicated xanthan with Debye parameter κ in bulk solution. Experimental data represented by symbols are provided to compare with the results by BD simulations. The error bars represent the standard deviation.

ment. When performing the image analysis, we set up the desirable range of fluorescence intensity and ignore xanthan molecules that appear too dim due to an escape from the focal plane, which has a conflict with the 2D translational diffusion. The microscope allows observing the motion of xanthan chain in the focal plane of the chamber in the x-y direction, as provided in Fig. 4. In this, the focal plane is possible to locate with a minimum adjustment of 50 nm by means of the precise z-axis focus module.

IV. RESULTS AND DISCUSSION

A. Image analysis of fluorescein-labeled xanthan molecule

After subtracting the background, a threshold was set in order to divide the image into subframes encompassing a single xanthan molecule. The zeroth moment accounts for the total intensity $I(t)$ of a single molecule, which can be calculated from the intensity distribution function $I(\mathbf{r},t)$ of a pixel with a set of coordinates $\mathbf{r}$,

$$I(t) = \int I(\mathbf{r},t)d\mathbf{r}. \tag{12}$$

Here, $I(t)$ is $\Sigma_{p,q}I_{pq}(t)$ with the fluorescent intensity I_{pq} of the pixel $\{p,q\}$, and we assume that the fluorescent label is uniformly distributed within a molecule. The first moment of the intensity distribution denotes the position of the center of mass

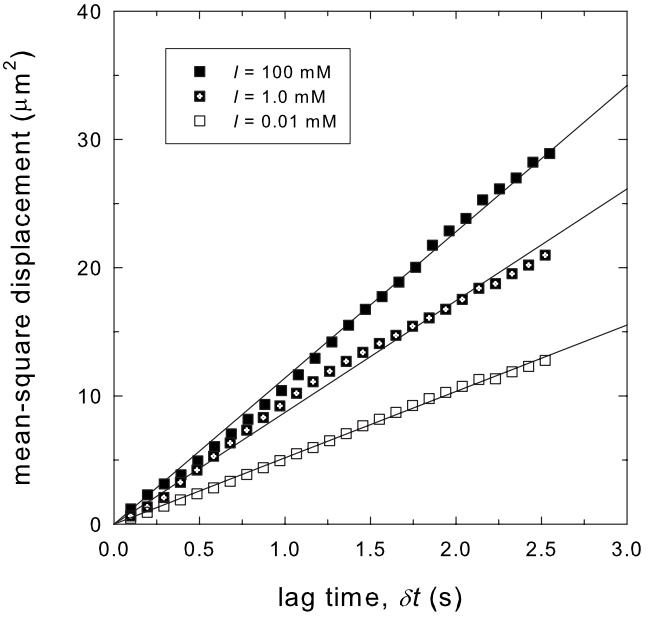

FIG. 9. The MSDs $\langle R_{CM}^2(t)\rangle$ of center of mass vs lag time. Each curve represents the average of 5 submovies and the frame rate for data is 10 frames/s.

$$\mathbf{R}_{CM}(t) = \frac{1}{I(t)}\int \mathbf{r}I(\mathbf{r},t)d\mathbf{r} \cong \frac{1}{I(t)}\sum_{p,q} Ir_{pq}(t)_{pq}(t). \tag{13}$$

Subsequently, the second moment determines the radius of gyration tensor, given by

$$G_{ij}(t) = \frac{1}{I(t)}\int (\mathbf{r}_i - \mathbf{R}_{CM,i})(\mathbf{r}_j - \mathbf{R}_{CM,j})I(\mathbf{r},t)d\mathbf{r}. \tag{14}$$

For x and y directions, Eq. (14) is expressed as

$$G_{xy}(t) \cong \frac{1}{I(t)}\sum [r_{pq,x}(t) - R_{CM,x}(t)][r_{pq,y}(t) - R_{CM,y}(t)]I_{pq}(t), \tag{15}$$

then the common radius of gyration can be obtained as

$$R_G^2(t) = trace(G_{xy}). \tag{16}$$

The instantaneous evolution of each moment can be obtained from the analysis of the acquired images by tracking with more than 20 xanthan. In Fig. 5, the zeroth moment giving the total fluorescence intensity $I(t)$ is almost constant over time with little fluctuations. Once the photobleaching is introduced, a systematic slow exponential decrease will be observed. According to the x and y components of the R_{CM}, the evolution of the R_G appears nearly unchanged. As a demonstrative example, the trajectories of center of mass (in the x-y plane) are shown in Fig. 6. Note that the displacement direction in each step is a random process exhibiting Brownian motion. We recognized that most of the displacements should have approximately the same length and its distribution becomes Gaussian.

B. Comparison between experiments and simulations

The change in chain dimension due to labeling was assessed from the behavior of the zeta potential and rheological property. In Table II, labeling with xanthan/fluorescein mass ratio of 300 mg/15 mg (molar ratio=6.29×10^{-3}) has no significant influence on the surface charge, indicating that the values of R_C and l_P are almost unchanged. However, the reduced behavior of intrinsic viscosity by the labeling should be considered to adjust another model parameter pertaining to the xanthan dimension. With a simplified assumption of the rod structure, a relationship between the viscosity factor $[\eta]/V_{sp}$ and high values (>50) of the aspect ratio $\lambda(=R_C/d)$ is possible to apply here by the power-law function as $[\eta]/V_{sp}\sim\lambda^{1.801}$, where V_{sp} is the specific volume of xanthan [40]. In Fig. 7, the ratio of λ between the unlabeled and labeled xanthan, $\lambda/\lambda_{label}=([\eta]/[\eta]_{label})^{1/1.801}$, increases with increasing κ. The value of the ratio d_{label}/d determined by λ/λ_{label} enables the labeling effect to be correct by estimation of the modified bead radius, on the basis of $(4\pi/3)(a^3N_b)=\pi(d/2)^2R_C$.

Figure 8 depicts the radius of gyration of the labeled xanthan with native and sonicated samples, where comparisons are shown between experimental results and the prediction by BD simulations. The simulation system, which is infinite in the x and y directions, is equilibrated for 2 ms (1×10^6 time steps) and the averages are taken for the next 14 ms (7×10^6 time steps). Owing to the lack of intrinsic rigidity, the flexible model exhibits a smaller size than the semiflexible model. With decreasing ionic strength (or κ), each xanthan chain extends and converges to a fully extended one which corresponds to a large increase in the experimental contour length. This property is represented by the fact that

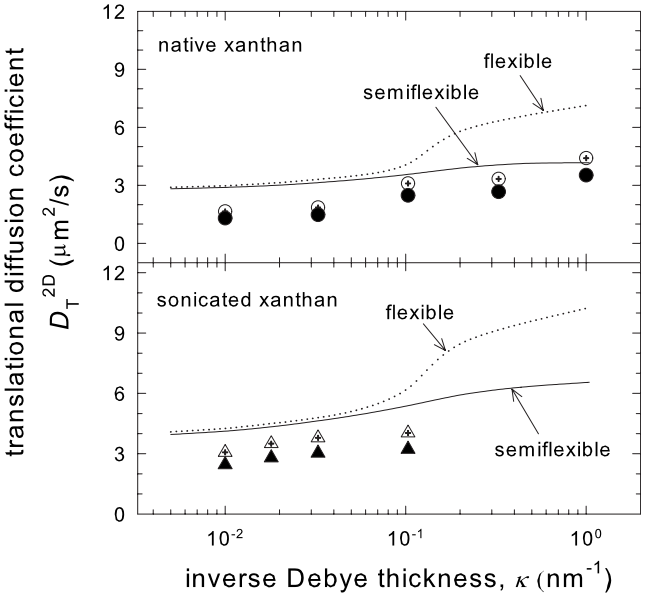

FIG. 10. The variations in the self-diffusion coefficient D_T^{2D} of a single native and 5 min sonicated xanthan with Debye parameter κ in bulk solution. Experimental data represented by symbols are provided to compare with the results by BD simulations. Solid symbols exhibit the pure 2D diffusion (D_T^{2D} in x and y directions only) and crossed open symbols exhibit the quasi-2D one ($=(D_T^{2D}+D_T^{3D})/2$).

$(R_E/R_G)^2=9.7$ for semiflexible model at $\kappa=0.01$ nm^{-1} could be close to the value 12 corresponding to the full extension, as described in a previous study. At high ionic strength (i.e., $I>10$ mM), the chain structure is nearly identical to that of the neutral chain. For the sonicated xanthan at $I>1.0$ mM, it is really hard to obtain an assured R_G value due to the limitation of magnification. In Fig. 8, experimental results have a reasonable trend to agree with the prediction by BD simulations. Our simulated R_G values can be compared with those previously reported in other studies [22,23,41] for dilute xanthan solutions, by combining the literature data overall. From the plot of R_G values as a function of the average molecular weight obtained by theoretical calculations and light-scattering measurements, each values of R_G in 5 g/L aqueous NaCl (i.e., $I=0.086$ M, $\kappa=1.04$ nm^{-1}) are found in the range of 120–140 and 80–100 nm for our native and 5 min sonicated xanthan, respectively. These ranges are consistent again with the results reported later [42].

As was noted in Eq. (11), the self-diffusion coefficient of the xanthan chain is determined from the MSD $\langle R_{CM}^2(t)\rangle$ with the lag time δt in each Brownian trajectory,

$$D_T^{2D}=\lim_{\delta t\to\infty}\frac{\langle R_{CM}^2(t)\rangle}{4\delta t}, \tag{17}$$

where

$$\langle R_{CM}^2(t)\rangle=\langle[R_{CM,x}(t)-R_{CM,x}(t-\delta t)]^2+[R_{CM,y}(t)-R_{CM,y}(t-\delta t)]^2\rangle. \tag{18}$$

After binning the trajectory into several segments, we calculated the center-of-mass displacement for each individual molecule within each segment as a function of the time elapsed between the frames in which the displacement was measured, as shown in Fig. 9. As expected, the MSD of the xanthan molecules increases linearly with lag time. The value of $\langle R_{CM}^2(t)\rangle/4\delta t$ is fairly constant except the initial stage. The in-plane diffusion coefficient was obtained from the slope of the MSD of the ensemble average vs lag time with 95% confidence, in which error estimates were made using the bootstrap method for lots of subensembles of molecule paths.

Figure 10 shows the self-diffusion coefficient D_T^{2D} of the labeled chain of native and sonicated xanthan with variations in the medium ionic strength. The values for each sample mostly converge to the single bead value $D_0=k_BT/6\pi\eta a$ at low ionic strength (or low κ). The self-diffusion increases with increasing κ since the chain becomes more compact, and a large difference in self-diffusion between the flexible and semiflexible chains at high κ is attributed to the size difference shown in Fig. 8. In Fig. 10, although the consistent trend of the data is evident, the experimental diffusion coefficients show lower values than the simulation results. Although we select to identify and analyze only the particles within a certain desirable intensity range, it should rely on intuition in some extent because the effective size of xanthan molecule is actually in the limited range, in view of the pixel size of our system. Inferring this uncertainty in the complete 2D image tracking, the values of quasi-2D translational diffusion coefficient shown as open symbols are estimated by

meaning D_T^{2D} and D_T^{3D}. Further, we compare our simulated D_T^{2D} with those reported in the literature. The D_T^{2D} value of xanthan with $\bar{M}_W$ of 1.8×10^6 in 5 g/L aqueous NaCl was measured as 2.5×10^{-8} cm^2/s at infinite dilution [41]. More significant data should be recognized by the D_T^{2D} plot of the fluorescein-labeled xanthan in dilute regime provided by Tinland *et al.*[42], from which we can verify our native and 5 min sonicated xanthan as corresponding to about 5×10^{-8} and 7×10^{-8} cm^2/s, respectively.

Each discrepancy between the BD simulation and experimental results could be estimated as the average relative differences with respect to the simulation values of the radius of gyration and translational diffusion coefficient, as provided in Fig. 11. Simulation results of the radius of gyration can be compared well to experiments, showing a discrepancy of less than about 30%. In the translational diffusion, the simulation prediction is higher than the experimental measurements for the entire range of ionic concentration, with the relative difference in the level of up to about 45%. Considering the fact that literature data agree well with the simulations rather than the fluorescent tracking results, a main cause of the discrepancy might be due to limitations in experiments such as the incomplete 2D image tracking. In addition, we need to pursue more rigorous parameter set, which can be obtained by applying more advantageous experimental methods to characterize the fluorescein-labeled xanthan. It will be one of the main tasks for further investigation in the near future.

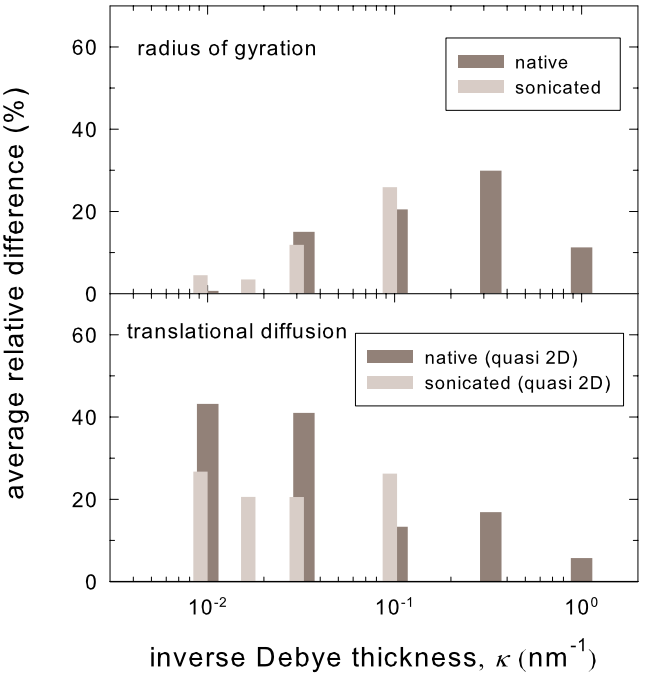

FIG. 11. (Color online) The relative differences in values of the radius of gyration and translational diffusion of native and sonicated xanthan between experimental measurements and simulation results of semiflexible chain.

V. CONCLUDING REMARKS

The use of anionic polysaccharide xanthan allows the application of direct visualization to quantify the structure and diffusion of an individual polyelectrolyte chain. From the BD simulations of native and sonicated xanthan in bulk solution, we found that the structure and diffusion of polyelectrolyte chains depend sensitively on the medium ionic strength, in which their dependency agrees well with the semiflexible wormlike chain model. The change in bead radius due to the labeling, based on the rheological behavior of the intrinsic viscosity, was properly implemented by combining with optimized model parameters for unlabeled xanthan. It is evident that our BD simulation is tending toward qualitative agreement with experiments. However, the experimental diffusion coefficients reveal lower values than the simulation results. A proper explanation for the discrepancy should be given as a choice of the parameter set for labeled xanthan characteristics and the incomplete 2D image tracking for translational diffusion. Despite these restrictions, the consistency with literature values confirms the validity of our BD simulations that model rigorously experimental systems of the single polyelectrolyte. Our experimental verification with xanthan in bulk solution is important for polyelectrolyte molecules in confined spaces. The self-diffusion coefficient provides important information on the chain structure as well as dynamics.

ACKNOWLEDGMENTS

This work was supported by Nanotechnology Research Fund (Grant No. 2008-02344) from the Korea Science and Engineering Foundations as well as Future-Oriented Research Fund (Grant No. 2E20590) from the Korea Institute of Science and Technology (KIST). We also acknowledge the support of BK21 Program provided to D.E.L.

[1] K. Kremer and K. Binder, Comput. Phys. Rep. **7**, 259 (1988).
[2] D. A. Hoagland and M. Muthukumar, Macromolecules **25**, 6696 (1992).
[3] *Electrostatic Effects in Soft Matter and Biophysics*, NATO Science Series II: Mathematics, Physics and Chemistry, edited by C. Holm, P. Këkicheff, and R. Podgornik (Kluwer, Dordrecht, 2001), Vol. 46.
[4] M. Daoud and P.-G. de Gennes, J. Phys. (France) **38**, 85 (1977).
[5] J. H. van Vliet and G. ten Brinke, J. Chem. Phys. **93**, 1436 (1990).
[6] J.-L. Barrat and J.-F. Joanny, Adv. Chem. Phys. **94**, 1 (1996).
[7] A. V. Dobrynin and M. Rubinstein, Prog. Polym. Sci. **30**, 1049 (2005).
[8] H. C. Öttinger, *Stochastic Processes in Polymeric Fluids: Tools and Examples for Developing Simulation Algorithms*

(Springer, Heidelberg, 1996).
[9] H. A. Jian, V. Vologodskii, and T. Schlick, J. Comput. Phys. **136**, 168 (1997).
[10] J. S. Hur, E. S. G. Shaqfeh, and R. G. Larson, J. Rheol. **44**, 713 (2000).
[11] R. M. Jendrejack, D. C. Schwartz, M. D. Graham, and J. J. de Pablo, J. Chem. Phys. **119**, 1165 (2003).
[12] R. M. D. Jendrejack, D. C. Schwartz, J. J. de Pablo, and M. D. Graham, J. Chem. Phys. **120**, 2513 (2004).
[13] Y. L. Chen, M. D. Graham, J. J. de Pablo, G. C. Randall, M. Gupta, and P. S. Doyle, Phys. Rev. E **70**, 060901(R) (2004).
[14] D. E. Smith, T. T. Perkins, and S. Chu, Macromolecules **29**, 1372 (1996).
[15] C. Haber, S. A. Ruiz, and D. Wirtz, Proc. Natl. Acad. Sci. U.S.A. **97**, 10792 (2000).
[16] B. Maier and J. O. Rädler, Phys. Rev. Lett. **82**, 1911 (1999).
[17] B. Maier and J. O. Rädler, Macromolecules **33**, 7185 (2000).
[18] B. Maier and J. O. Rädler, Macromolecules **34**, 5723 (2001).
[19] A. Balducci, P. Mao, J. Han, and P. S. Doyle, Macromolecules **39**, 6273 (2006).
[20] P.-K. Lin, C.-C. Fu, Y.-L. Chen, Y.-R. Chen, P.-K. Wei, C. H. Kuan, and W. S. Fann, Phys. Rev. E **76**, 011806 (2007).
[21] J. Jeon and M.-S. Chun, J. Chem. Phys. **126**, 154904 (2007).
[22] G. Paradossi and D. A. Brant, Macromolecules **15**, 874 (1982).
[23] T. Sato, T. Norisuye, and H. Fujita, Macromolecules **17**, 2696 (1984).
[24] M.-S. Chun and O. O. Park, Macromol. Chem. Phys. **195**, 701 (1994).
[25] D. L. Ermak and J. A. McCammon, J. Chem. Phys. **69**, 1352 (1978).
[26] J. Rotne and S. Prager, J. Chem. Phys. **50**, 4831 (1969).
[27] H. R. Warner, Ind. Eng. Chem. Fundam. **11**, 379 (1972).
[28] B. T. Stokke, A. Elgsaeter, G. Skjåk-Brjek, and O. Smidsrød, Carbohydr. Res. **160**, 13 (1987).
[29] G. S. Manning, J. Chem. Phys. **51**, 924 (1969).
[30] A. Dhar and D. Chaudhuri, Phys. Rev. Lett. **89**, 065502 (2002).
[31] M. Doi and S. F. Edwards, *The Theory of Polymer Dynamics* (Clarendon, Oxford, 1986).
[32] B. Li, N. Madras, and A. D. Sokal, J. Stat. Phys. **80**, 661 (1995).
[33] B. Dünweg and K. Kremer, J. Chem. Phys. **99**, 6983 (1993).
[34] H. Yamakawa and T. Yoshizaki, Macromolecules **13**, 633 (1980).
[35] T. Odijk, J. Polym. Sci., Polym. Phys. Ed. **15**, 477 (1977).
[36] J. Skolnick and M. Fixman, Macromolecules **10**, 944 (1977).
[37] T. A. Camesano and K. J. Wilkinson, Biomacromolecules **2**, 1184 (2001).
[38] W. E. Rochefort and S. Middleman, J. Rheol. **31**, 337 (1987).
[39] G. Holzwarth, Carbohydr. Res. **66**, 173 (1978).
[40] Y. Layec and C. Wolff, Rheol. Acta **13**, 696 (1974).
[41] G. Muller, J. Lecourtier, G. Chauveteau, and C. Allain, Makromol. Chem., Rapid Commun. **5**, 203 (1984).
[42] B. Tinland, G. Maret, and M. Rinaudo, Macromolecules **23**, 596 (1990).